Polarization Dependent High Energy Resolution X-ray Absorption Study of Dicesium Uranyl Tetrachloride

10 AUTHORS, INCLUDING:

Jennifer C Green
University of Oxford

393 PUBLICATIONS **8,774** CITATIONS

SEE PROFILE

Kevin Jorissen
University of Washington Seattle

28 PUBLICATIONS **365** CITATIONS

SEE PROFILE

J. J. Rehr
University of Washington Seattle

410 PUBLICATIONS **18,606** CITATIONS

SEE PROFILE

Melissa Anne Denecke
The University of Manchester
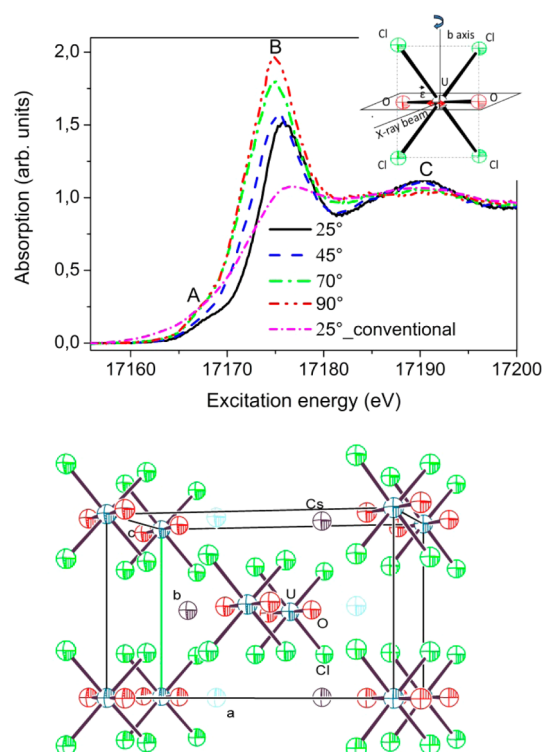
184 PUBLICATIONS **2,694** CITATIONS

SEE PROFILE

Inorganic Chemistry

Polarization Dependent High Energy Resolution X-ray Absorption Study of Dicesium Uranyl Tetrachloride

Tonya Vitova,*,[†] Jennifer C. Green,[‡] Robert G. Denning,[‡] Matthias Löble,[†] Kristina Kvashnina,[§] Joshua J. Kas,[∥] Kevin Jorissen,[∥] John J. Rehr,[∥] Thomas Malcherek,[⊥] and Melissa A. Denecke[†,△]

[†]Karlsruhe Institute of Technology, Institute for Nuclear Waste Disposal, P.O. Box 3640, 76021 Karlsruhe, Germany

[‡]Department of Chemistry, Oxford University, South Parks Road, Oxford OX1 3QR, U.K.

[§]European Synchrotron Radiation Facility (ESRF), 6 Rue Jules Horowitz, BP 220, 38043 Grenoble Cedex 9, France

[∥]Department of Physics, University of Washington, Seattle, Washington 98195, United States

[⊥]Department of Geosciences, University of Hamburg, Grindelallee 48, 20146 Hamburg, Germany

Ⓢ Supporting Information

ABSTRACT: Dicesium uranyl tetrachloride ($Cs_2UO_2Cl_4$) has been a model compound for experimental and theoretical studies of electronic structure of U(VI) in the form of UO_2^{2+} (uranyl ion) for decades. We have obtained angle-resolved electronic structure information for oriented $Cs_2UO_2Cl_4$ crystal, specifically relative energies of 5f and 6d valence orbitals probed with extraordinary energy resolution by polarization dependent high energy resolution X-ray absorption near edge structure (PD-HR-XANES) and compare these with predictions from quantum chemical Amsterdam density functional theory (ADF) and ab initio real space multiple-scattering Green's function based FEFF codes. The obtained results have fundamental value but also demonstrate an experimental approach, which offers great potential to benchmark and drive improvement in theoretical calculations of electronic structures of actinide elements.

1. INTRODUCTION

The physics and chemistry of uranium plays a central role in the safety assessment of a nuclear waste repository and reduction of the radiotoxicity of spent nuclear fuel, which are of fundamental importance for safe and sustainable use of nuclear energy. Detailed knowledge about the U oxidation state and electronic structure is necessary to predict its reactivity, which determines U mobilization/immobilization behavior in the environment, for example, in case of water intrusion in a deep geological repository.[1] Furthermore, insight into actinide (An) electronic structure facilitates understanding and ultimately fine-tuning N-donor ligand selectivity for An over their chemically similar lanthanide (Ln) analogs necessary for separating An from Ln in a key step in the so-called partitioning and transmutation (P&T) strategy for reduction the radio-toxicity of spent nuclear fuel.[2] Despite numerous experimental and theoretical studies, the electronic structure of U(VI) (mostly present as the UO_2^{2+} uranyl ion) remains subject of discussion.[3−6]

The uranyl moiety is highly symmetric with linear structure with unusually short, strong covalent bonding to two axial O atoms. The linear structure leads to the U valence orbitals being most usefully described in terms of their σ, π, δ, or ϕ character with respect to rotation about the U−O z-axis. Introduction of four Cl groups along the x and y axes, giving D_{4h} symmetry, lifts the degeneracy of the δ symmetry orbitals. The residual doubly degenerate U orbitals when singly occupied experience strong spin−orbit coupling and the resultant orbital energy manifold needs inclusion of this effect to account for the ordering. The axial nature of the uranyl ion leads to anisotropic character and a strong polarization dependency of the uranyl X-ray absorption spectroscopy (XAS) signal.[7,8] In this study, the aim is to extend the current knowledge about the electronic structure of $UO_2Cl_4^{2-}$. The relative energies of the occupied and unoccupied $UO_2Cl_4^{2-}$ valence molecular orbitals with 5f and 6d character derived from optical experiments and XAS have been extensively reviewed and compared to scalar relativistic zeroth order regular approximation (ZORA) density functional theory (DFT) calculations employing the BP86 functional.[5,9] We compare the relative energies of the unoccupied $UO_2Cl_4^{2-}$ 5f- and 6d-based valence orbitals calculated with Amsterdam density functional theory (ADF)[10] code with those measured from experimental U L_3-edge high energy resolution polarization dependent X-ray absorption near edge structure (PD-HR-XANES) of a dicesium uranyl tetrachloride ($Cs_2UO_2Cl_4$) crystal grown along the b crystallographic axis (see Figure 1 bottom). Selective transitions to U 5f

Figure 1. U L_3-edge PD-HR-XANES and a conventional PD-XANES of $Cs_2UO_2Cl_4$ (top) for different angles between the uranyl moiety UO_2^{2+} and the polarization vector of the incident X-ray beam ε (top, inset); the unit cell of $Cs_2UO_2Cl_4$ (bottom).

71 or 6d valence orbitals (U $2p_{3/2} \rightarrow$ 5f/6d) are detected in the
72 same U L_3-edge PD-HR-XANES spectrum with remarkable
73 energy resolution. The experimental observations combined
74 with theoretical results allow qualitative evaluation of the level
75 of mixing of O, Cl, and U valence orbitals. The U L_3-edge PD-
76 HR-XANES spectra are also successfully reproduced by ab
77 initio real space multiple-scattering Green's function based
78 theoretical FEFF9.6 code calculations.[11] The relative energy
79 positions of U $3d_{3/2} \rightarrow$ 5f electronic transitions experimentally
80 probed by U M_4-edge PD-HR-XANES are also discussed in
81 comparison to the ADF results.

2. EXPERIMENTAL DETAILS

82 **2.1. Preparation and Characterization of Dicesium Uranyl**
83 **Tetrachloride ($Cs_2UO_2Cl_4$).[12]** $Cs_2UO_2Cl_4$ was prepared from
84 uranylacetate and cesium chloride. For the preparation of
85 uranylacetate ($UO_2(CH_3CO_2)_2$) $UO_2(NO_3)_2$ (1 g, 2.5 mmol) was
86 dissolved in water and heated to 100 °C. An excess of ammonium
87 chloride (3 g) was added to the boiling solution and the pH-value
88 adjusted with concentrated ammonia. Yellow flakes of ammonium-
89 diuranate precipitated after it was cooled to room temperature. After the
90 overlaying solution was decanted, the yellow precipitate was washed
91 with water several times (8−9 mL). The precipitate was then dried at
92 80−100 °C and the resulting product ground in mortar and pestle.
93 The resulting yellow powder was calcined under ambient atmosphere
94 at 350 °C for 12 h to obtain an oxide. The red product was suspended
95 in water (30 mL), heated to 80 °C and dissolved in 10 mL
96 concentrated acetic acid. The hot solution was filtered and the filtrate
97 cooled down to room temperature. After standing overnight, yellow
98 rod shaped crystals of $UO_2(CH_3COO)_2$ 2 H_2O were isolated. The
99 crystals were washed with dilute acetic acid and dried at room
100 temperature in air. (Yield: 634 mg, 1.6 mmol, 64%). Yellow crystalline
101 $UO_2(CH_3COO)_2 \cdot 2H_2O$ (500 mg, 1.2 mmol) was dissolved in 10 mL
102 of hot dilute HCl and a stochiometric amount of CsCl added. After

103 cooling to room temperature, the precipitated product was isolated
104 and recrystallized from dilute hydrochloric acid solution. The yellow
105 crystalline $Cs_2UO_2Cl_4$, with rod crystallites grown along the b
106 crystallographic axis (see Figure 1) were filtered and dried at room
107 temperature in air (yield = 212 mg, 0.31 mmol, 25.8%).

108 Face indices of a selected $Cs_2UO_2Cl_4$ crystal were determined using
109 single crystal X-ray diffraction (Nonius KappaCCD, graphite
110 monochromated Mo Kα radiation). The obtained orientation matrix
111 yields monoclinic lattice parameters $a = 11.903$ Å, $b = 7.682$ Å, $c =$
112 5.771 Å, $\beta = 100.15°$, $V = 519.44$ Å^3, Observed deviations from the
113 lattice parameters reported in the Inorganic Crystal Structure Database
114 (ICSD), entry 39490, $a = 12.0058$, $b = 7.6973$, $c = 5.8503$, $\beta = 100.0°$, V
115 = 532.34 Å^3, space group C1m1, might be attributed to absorption
116 effects caused by the large crystal size. These are of no significance for
117 the results obtained for actual $Cs_2UO_2Cl_4$ crystal employed here.

118 **2.2. XAS Experiments.** The XAS experiments at the U L_3- (17166
119 eV), and M_4-edge (3728 eV) of a $Cs_2UO_2C_4$ crystal with approximate
120 dimensions $0.5 \times 0.5 \times 5$ mm were performed at the ID26 beamline at
121 the European Synchrotron Radiation Facility (ESRF), Grenoble,
122 France. The synchrotron radiation was monochromatized by a Si(311)
123 (U L_3)/Si(111) (U M_4) double crystal monochromator (DCM).
124 Rejection of higher harmonics was achieved by two Pd/Cr (U L_3)/Si
125 (U M_4) mirrors working under total reflection. The energy calibration
126 was performed assigning 17998/4966 eV to the first inflection point of
127 a Zr K edge (U L_3)/Ti K edge (U M_4) XANES spectrum. All reported
128 experiments were performed at room temperature.

129 U L_3 edge extended X-ray absorption fine structure (EXAFS)
130 spectra were measured in fluorescence mode using an avalanche
131 photodiode (APD).

132 During the PD-HR-XANES measurements for each excitation
133 energy the U Lα_1 (13614 eV)/Mß (3339.8 eV) emission was selected
134 by a spherically bent Ge(777)/Si(220) analyzer crystal and focused on
135 an APD (U L_3)/single pixel silicon drift detector (SDD) KETEK (U
136 M_4). The sample, crystal, and detector were positioned on a circle
137 (Rowland geometry) with diameter 1 m equal to the bending radius of
138 the crystal.[13] A combined incident convoluted with emitted energy
139 resolution of 1.8 eV (U L_3)/0.8 eV(U M_4) was estimated by measuring
140 the full width at half-maximum of the quasi-elastic peak. During the U
141 M_4-edge experiments a polyethylene balloon filled with He and
142 equipped with three 10 μm thick polyethylene windows was placed
143 between sample, analyzer crystal, and detector to avoid absorption of
144 low energy Mß fluorescence photons by air.

145 U L_3/M_4-edge PD-HR-XANES/U L_3 EXAFS measurements were
146 performed for 25° (EXAFS), 45°, 70°, and 90° (EXAFS) (U L_3) and α
147 = $\alpha_1 + 5°$ (0° ≤ α_1 ≤ 45°), $\alpha + 10°$, $\alpha + 20°$, $\alpha + 30°$, and $\alpha + 40°$ (U
148 M_4) orientation of the uranyl moiety UO_2^{2+} in the crystal with respect
149 to the polarization vector ε of the primary beam (rotation around the b
150 crystal axis, which corresponds to the long side of the crystal) (see
151 Figure 1). For the U M_4 measurements the initial angle (α) between ε
152 and UO_2^{2+} was not precisely determined; therefore a parameter α_1,
153 which can have value within the interval 0° ≤ α_1 ≤ 45° is introduced.
154 The orientation notations are used in the manuscript. The energy of
155 the incident beam was scanned from 17151.2/16785 to 17225.2/
156 17853 eV with 0.1/1 eV step size, 600/100 s per HR-XANES/EXAFS
157 spectrum, over the U L_3-edge and from 3715 to 3750 eV with 0.1 eV
158 step size, 60 s per HR-XANES over the U M_4-edge. At least three
159 spectra for each angle were collected in order to check the
160 reproducibility of the spectral features and to improve the counting
161 statistics. The measured spectra showed no occurrence of radiation
162 damage.

163 U L_3-edge EXAFS measurement of a powder $Cs_2UO_2Cl_4$ sample is
164 performed at the INE-Beamline for actinide research at ANKA
165 synchrotron radiation facility, Karlsruhe, Germany. See the Supporting
166 Information for experimental details and details on the analyses of all
167 EXAFS data.

168 Linear combination least-squares (LCLS) fit analyses of the U L_3-
169 and M_4-edge PD-HR-XANES spectra of $Cs_2UO_2Cl_4$ were performed
170 with the WINXAS program (www.winxas.de) using three (U L_3) or
171 five (U M_4) pseudo-Voigt (PV) [$f(x) = \alpha$Gaussian + (1 −

172 α)Lorentzian] and one arctangent functions. The Levenberg–
173 Marquardt least-squares algorithm is used in the fit.

2.3. Computational Details. *2.3.1. ADF.* The calculations
175 presented in section 3.2 used the Amsterdam Density Functional
176 program suite,[14] ADF2000.2.[15] An uncontracted triple-ζ basis set of
177 Slater type orbitals was used with two additional polarization functions
178 for O and Cl (ADF type V). Scalar relativistic corrections were
179 included via the ZORA method.[16] All electrons were included. The
180 local density parametrization of Vosko, Wilk, and Nusair[17] was
181 employed, with exchange and correlation corrections as advocated by
182 Becke in 1988,[18] and Perdew in 1986,[19] respectively. From the
183 eigenvectors of a ADF calculation, we obtained the radial amplitude of
184 the orbitals involved in the U L_3-edge PD-HR-XANES transitions (see
185 Supporting Information Figure S1). Notice the very small amplitude of
186 the 7s orbital in the region where that of $2p_{3/2}$ is large, and also the
187 extensive cancellation where these functions overlap. As a result the
188 $R_{2p/7s}^{(1)}$ integral is too small to provide significant intensity in XANES.
189 The radial extent of the $2p_{3/2}$ shell is critical in the calculation of the
190 transition moments so the characteristics of the orbitals obtained using
191 an ADF calculation that includes the spin–orbit interaction, are
192 compared with those from a full relativistic Hartree–Fock calculation,
193 as tabulated by Desclaux. Excellent agreement is obtained for the
194 average value of various powers of r, so the eigenfunctions from the
195 ADF calculation were used with confidence for the calculation of the
196 radial integrals.

197 *2.3.2. FEFF9.6.* The U L_3-edge $Cs_2UO_2Cl_4$ PD-HR-XANES spectra
198 and the O, Cl, and U density of states were calculated with the
199 FEFF9.6 ab initio quantum chemical code based on the multiple
200 scattering theory.[11] The potentials of free atoms were calculated with a
201 relativistic Dirac–Fock atom code part of FEFF9.6. The scattering
202 potentials were calculated self-consistently by overlapping the free
203 atomic density in the muffin tin approximation within a cluster of 149
204 atoms (SCF card). The UNFREEZEF card was used to include the U f
205 states in the SCF calculation providing their accurate energy
206 position.[20] The energy dependent exchange Hedin–Lundquist
207 potential was used for the fine structure and the atomic background
208 (EXCHANGE card). The Fermi energy was corrected by 2 eV to
209 lower energies and the core-hole lifetime broadening was reduced by
210 2.5 eV leading to a broadening of 5.6 eV. The full multiple scattering
211 XANES spectra were calculated for an atomic cluster of 228 atoms
212 centered on the absorbing U atom (FMS and XANES cards). Best
213 agreement between calculation and experiment was found by applying
214 "COREHOLE RPA" option to screen the $2p_{5/2}$ core-hole. The
215 orientation of the vector of polarization of the incident mono-
216 chromatic radiation (ε) parallel or perpendicular to the UO_2^{2+}
217 molecular axis was achieved by using the POLARIZATION card.
218 The spectra were calculated for dipole or dipole and quadrupole
219 electronic transitions (MULTIPOLE card). Note that "MULTIPOLE
220 2" in combination with the POLARIZATION card is only possible by
221 using the ELLIPTICITY card depicting perpendicular orientation of ε
222 with respect to the incident beam denoting linearly polarized incident
223 X-ray beam.

3. RESULTS AND DISCUSSION

224 **3.1. Experiment.** The U L_3-edge PD-HR-XANES spectra
225 of a $Cs_2UO_2Cl_4$ crystal for 25°, 45°, 70°, and 90° orientation of
226 the uranyl moiety with respect to the linear polarization vector
227 ε of the incident X-ray beam (inset in Figure 1) and
228 conventionally measured PD-XANES for 25° are shown in
229 Figure 1. The absorption resonances (A, B, C) of the PD-HR-
230 XANES spectra are more resolved in energy compared to the
231 25° conventional PD-XANES because of reduced core-hole
232 lifetime broadening effects.[21] An additional resonance A is
233 detected and B and C resonances are well-separated in all PD-
234 HR-XANES. The width narrowing of the U L_3-edge spectral
235 features reduces uncertainties of energy positions, intensities
236 and areas of the A, B and C features modeled by pseudo-Voigt
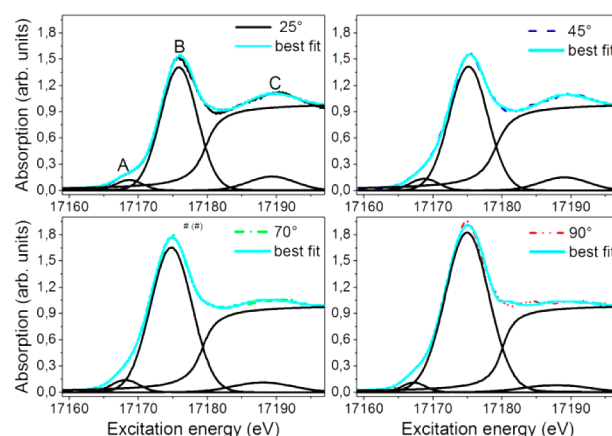237 (PV) profiles (see Figure 2, Table 1). The observed pre-edge

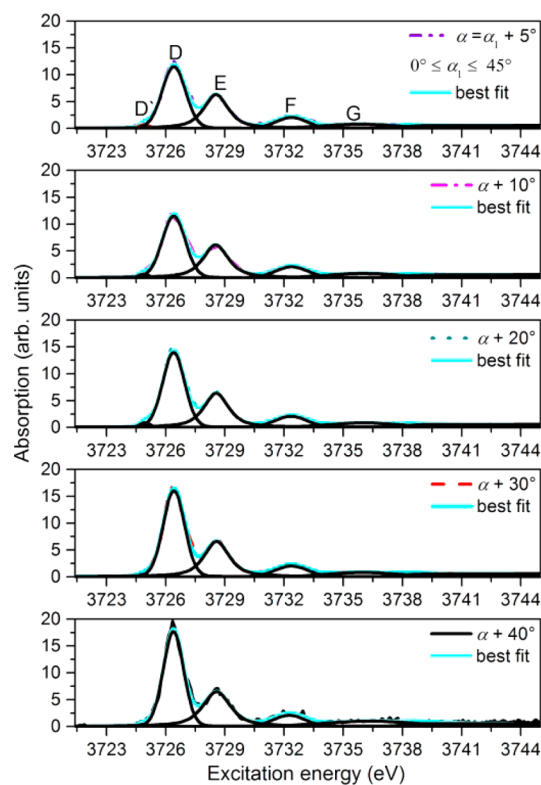**Figure 2.** U L_3-edge PD-HR-XANES spectra and fits of $Cs_2UO_2Cl_4$;
three PV and an arctangent functions used in the LCLS fit analyses
(see Table 1).

feature A, previously assigned to $2p_{3/2} \rightarrow 5f$ quadrupole allowed
electronic transitions for U(VI) materials,[22] shifts by −1.5 eV ±
0.1 eV to lower energy for the 90° compared to the 25°
spectrum. The most pronounced absorption resonance B
(white line, WL) describes dipole allowed $2p_{3/2} \rightarrow 6d$
electronic transitions. Previous conventional PD-XAS studies
of a $RbUO_2(NO_3)_3$ single crystal reports predominant
transitions to $6d\delta$ and $6d\pi$ orbitals in this spectral area for
90° and 0° orientation, respectively.[5,9] In Figure 1, the WL
shifts −0.9 ± 0.1 eV to lower energies and its integral intensity
increases going from the 25° to the 90° spectrum.

The postedge absorption resonance C gains intensity and
area approaching a 0° angle between linear UO_2^{2+} units and ε
due to an increasing contribution of photoelectron multiple
scattering along O axial atoms.[7,8]

The U M_4-edge PD-HR-XANES spectra measured for angles
$\alpha = \alpha_1 + 5°$ ($0° \leq \alpha_1 \leq 45°$), $\alpha + 10°$, $\alpha + 20°$, $\alpha + 30°$, and $\alpha +$
40° orientation of the uranyl moiety with respect to ε of the
incident X-ray beam are shown in Figure 3. The absorption
resonance marked E is not resolved in the conventional U M_4-
edge XANES spectrum.[20,23,24]

The M_4-edge $3d_{3/2} \rightarrow 5f$ electronic transitions probe
unoccupied orbitals with predominant U 5f character.
Previously performed DFT calculations suggest that the first
intense peak D describes transitions to U $5f\delta$ and $5f\phi$
orbitals.[5,9,24] Peaks E and F are shifted by 2.2 ± 0.1 and 6 ±
0.1 eV to higher energy compared to peak D (see Figure 4 and
Table 2) and probe U $5f\pi$ and $5f\sigma$ orbitals, respectively.[5,9,24] It
was estimated from optical spectroscopy data that $5f\delta$ and $5f\phi$
should be separated by about 0.3 eV,[5] whereas about 0.6 eV
energy difference is resolved in our experimental data,
manifested by an asymmetric shape of the D peak in the U
M_4-edge PD-HR-XANES $\alpha = \alpha_1 + 5°$ ($0° \leq \alpha_1 \leq 45°$)
spectrum (see Supporting Information Figure S5). $5f\delta_{3/2}$ and
$5f\phi_{3/2}$ are nearly degenerate as well as $5f\delta_{5/2}$ and $5f\phi_{7/2}$ (see
Table 4 and Figure 5). The $5f\pi$ orbital should be shifted by
about 2.2 eV from $5f\delta$ and $5f\phi$ and this agrees with our
experimental observations.[4,5] O K-edge XANES results report
about 2.7 eV energy difference between the U $5f\sigma$ and $5f\pi$
orbitals,[5,9] whereas we find about 3.8 eV (see Figure 4 and
Table 2). The discrepancy of about 1 eV might be attributed to
different screening of the O 1s core-hole in the O K-edge
XANES compared to the U $3d_{3/2}$ core-hole in the U M_4-edge
PD-HR-XANES. The U $5f\delta$ and $5f\phi$ orbitals are nonbonding

Table 1. Name of Spectrum and Absorption Feature, Height, Position, and Full Width at Half Maximum (FWHM) Parameters of the PV Functions Used to Model the U L$_3$-edge PD-HR-XANES Spectra and an Arctangent Used to Model the Edge Jump, the Gauss Part (Gauss Part α) and the Area of the PV Profiles, and the Residual between Experimental Data and Best Fit

spectrum	feature	height ± 0.01	position ± 0.1 (eV)	fwhm ± 0.1 (eV)	gauss part α	area of PV	residual (%)
25°	A	0.12	17168.7	4.7	1[a]	0.6	2.6
45°	A	0.13	17168.8	4.8	1[a]	0.7	1.7
70°	A	0.14	17168.1	4.7	1[a]	0.7	1.8
90°	A	0.11	17167.2	4.0	1[a]	0.5	2.1
25°	B	1.41	17175.9	6.3	1[a]	9.5	2.6
45°	B	1.41	17175.2	6.6	1[a]	9.9	1.7
70°	B	1.65	17174.8	7.0	1[a]	12.4	1.8
90°	B	1.82	17175.0	7.5	1[a]	14.7	2.1
25°	C	0.16	17189.4	8.0	1[a]	1.3	2.6
45°	C	0.15	17189.1	8.1	1[a]	1.3	1.7
70°	C	0.11	17188.1	10.2	1[a]	1.2	1.8
90°	C	0.08	17187.9	11.3	1[a]	0.9	2.1
25°	arctan	1[a]	17179.8	5.3		18.4	2.6
45°	arctan	1[a]	17179.2	5.6		18.1	1.7
70°	arctan	1[a]	17179.3	5.0		19.5	1.8
90°	arctan	1[a]	17180.1	4.2		16.8	2.1

[a]The parameter is fixed during the fit.
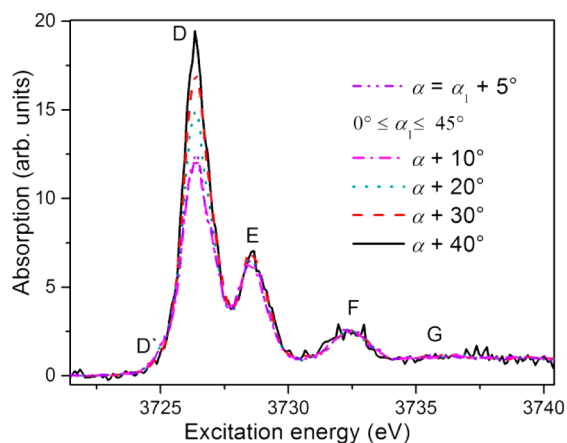
Figure 3. U M4-edge PD-HR-XANES spectra.

Figure 4. U M4-edge PD-HR-XANES spectra and fits of Cs$_2$UO$_2$Cl$_4$; five PV and an arctangent functions used in the LCLS fit analyses (see Table 2).

282 with respect to O with dominating 5f character.[4,5] There is
283 experimental and theoretical evidence for a relatively larger 5$f\sigma$
284 contribution to the U−O bond than of the 5$f\pi$ orbital, mainly
285 because of hybridization of the former with the 6$p\sigma$ orbital.[9]
286 Results from Cl K-edge XANES and DFT calculations report
287 that up to 8% Cl 3p character is mixed with the U 5$f\delta$, 5$f\phi$ and
288 5$f\pi$ orbitals.[6]

289 Polarization dependence is manifested mainly by a decrease
290 in area of the first intense absorption resonance D in case of α
291 = α_1 + 5° (0° ≤ α_1 ≤ 45°), compared to the α + 40° geometry
292 (see Figure 3). The energy positions of the D′, D, E, F, and G
293 features are not observed to be a function of ε within the
294 sensitivity of the measurements. No significant variations of
295 peak area for resonant features D′, E, and F is detected, as α
296 changes only by 40°. Such variations are demonstrated for 90°
297 and 0° geometries in quantum chemical calculations of U M$_5$-
298 edge PD-XANES of UO$_2$(NO$_3$)$_2$·6H$_2$O.[24]

299 **3.2. ZORA ADF Calculations.** To simulate the U L$_3$-edge
300 PD-HR-XANES spectra, the relative energies of the various
301 excited states are required. Figure 5 illustrates the steps in the
302 procedure for approximating these by means of a series of DFT
303 calculations. The z-axis corresponds to the 4-fold axis along the

U−O bonds and the four Cl atoms lie on the x and y axes. 304
Table 3 shows the relabeling of orbitals upon reducing 305 t3
symmetry from $D_{\infty h}$ to D_{4h} and inclusion of spin−orbit 306
coupling. The first column shows the virtual self-consistent field 307
(SCF) orbital energies for the electronic ground state of 308
UO$_2$Cl$_4^{2-}$, relative to that of the highest occupied molecular 309
orbital (HOMO), obtained using the ZORA that accounts for 310
scalar relativistic effects (Darwin and mass-velocity corrections) 311
but excludes the spin−orbit interaction. The third column 312

Table 2. Name of Spectrum and Absorption Feature, Height, Position, and Full Width at Half Maximum (FWHM) Parameters of the PV Functions Used to Model the U M$_4$ Edge PD-HR-XANES Spectra and an Arctangent Used to Model the Edge Jump, the Gauss Part (Gauss Part α) and the Area of the PV Profiles, and the Residual between Experimental Data and Best Fit

| spectrum	feature	height ± 0.01	position ±0.1 (eV)	fwhm ± 0.1 (eV)	gauss part α	area of PV	residual (%)
$\alpha + 40°$	D′	0.42	3724.9	0.6	1[a]	0.27	13.2
$\alpha + 30°$	D′	0.46	3724.9	0.5	1[a]	0.25	6.4
$\alpha + 20°$	D′	0.86	3725.0	0.6	1[a]	0.57	5.1
$\alpha + 10°$	D′	0.68	3724.9	0.6	1.0 ± 0.05	0.45	4.9
$\alpha = \alpha_1 + 5°$	D′	0.73	3724.9	0.6	1[a]	0.45	6.6
$\alpha + 40°$	D	17.77	3726.4	1.2	0.93[a]	23.5	13.2
$\alpha + 30°$	D	16.06	3726.4	1.3	0.93[a]	22.4	6.4
$\alpha + 20°$	D	13.98	3726.4	1.3	0.93[a]	20.0	5.1
$\alpha + 10°$	D	11.51	3726.4	1.4	0.93 ± 0.01	17.4	4.9
$\alpha = \alpha_1 + 5°$	D	11.54	3726.4	1.4	0.93[a]	17.6	6.6
$\alpha + 40°$	E	6.49	3728.6	1.7	0.3[a]	14.8	13.2
$\alpha + 30°$	E	6.63	3728.6	1.5	0.3[a]	13.8	6.4
$\alpha + 20°$	E	6.38	3728.6	1.5	0.3[a]	13.1	5.1
$\alpha + 10°$	E	6.12	3728.5	1.5	0.29 ± 0.01	12.9	4.9
$\alpha = \alpha_1 + 5°$	E	6.30	3728.5	1.5	0.3[a]	12.9	6.6
$\alpha + 40°$	F	2.08	3732.3	1.9	1[a]	4.2	13.2
$\alpha + 30°$	F	2.02	3732.4	2.0	1[a]	4.2	6.4
$\alpha + 20°$	F	2.05	3732.4	2.0	1[a]	4.3	5.1
$\alpha + 10°$	F	2.03	3732.4	2.0	1.0 ± 0.02	4.2	4.9
$\alpha = \alpha_1 + 5°$	F	2.03	3732.4	1.9	1[a]	4.0	6.6
$\alpha + 40°$	G	0.98	3736.3	5.7	0.94[a]	3.8	13.2
$\alpha + 30°$	G	0.81	3736.0	4.2	0.94[a]	3.7	6.4
$\alpha + 20°$	G	0.82	3736.0	4.4	0.94[a]	3.9	5.1
$\alpha + 10°$	G	0.79	3736.0	4.4	0.94 ± 0.02	3.8	4.9
$\alpha = \alpha_1 + 5°$	G	0.78	3735.8	4.5	0.94[a]	3.8	6.6
$\alpha + 40°$	arctan	0.60[a]	3738.0[a]	1.4[a]		7.0	13.2
$\alpha + 30°$	arctan	0.60[a]	3738.0[a]	1.4[a]		6.8	6.4
$\alpha + 20°$	arctan	0.60[a]	3738.0[a]	1.4[a]		6.8	5.1
$\alpha + 10°$	arctan	0.57 ± 0.01	3738.03 ± 0.01	1.44 ± 0.01		7.0	4.9
$\alpha = \alpha_1 + 5°$	arctan	0.60[a]	3738.0[a]	1.4[a]		7.0	6.6

[a]Parameter is fixed during the fit.
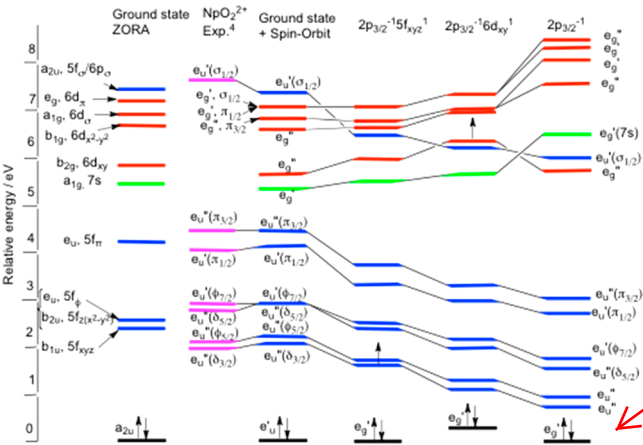
Figure 5. Theoretical SCF valence orbital energies showing the 6d orbitals (red), 5f (blue), and 7s (green) and their occupancy. The columns represent, from left to right, the ground state of $UO_2Cl_4^{2-}$ with scalar relativistic effects, the energy levels of NpO_2^{2+} from [4], the ground state of $UO_2Cl_4^{2-}$ with spin–orbit coupling included, the levels of $UO_2Cl_4^{2-}$ with a 2p to 5f excitation, the levels of $UO_2Cl_4^{2-}$ with a 2p to 6d excitation and the levels of $UO_2Cl_4^{1-}$ with a 2p electron ionized. The orbital labels are correlated in Table 3.

shows modifications introduced by the spin–orbit interaction and, in particular, the first order splitting of degenerate states with angular momentum about the O–U–O axis. These are quite small and the resulting 5f-electron levels are in satisfactory agreement with the f–f optical excitation energies observed in the $NpO_2Cl_4^{2-}$ ion[4] (second column). In addition, a core hole in an element has a similar effect on its valence levels as increasing the nuclear charge by one. Hence U with a core hole would be expected to have valence levels like Np. In the Np(V) system the spin–orbit splittings are somewhat larger, as one would expect for a metal with an additional nuclear charge, (cf., empirical coupling constants from atomic spectra, i.e., $\zeta_U = 1855$ cm^{-1} and $\zeta_{Np} = 2405$ cm^{-1}). The final three columns give virtual $2p_{3/2}$ core-hole configurations in which there is a hole in the $2p_{3/2}$ orbital and in which the valence electron is located in the 5f orbitals, in the $6d_{xy}$ orbitals or has been completely ionized. The main effect of the core hole is to stabilize the 5f orbitals relative to the 6d; this is clearly visible in the fully ionized case (right-hand column). This, in turn, influences the nature of the HOMO, which changes from e'_u to e'_g symmetry due to the 5f and 6d content of these ligand-based spinors. The relative stabilization of the 5f shell is, however, less pronounced when the excited electron is retained in a 5f orbital than when it occupies a 6d orbital; evidently the 5f electron screens the core hole more effectively than the penetrating 6d orbital, as might be anticipated from the distribution of their amplitudes in the core region (see Supporting Information Figure S1). The nonbonding components of these shells

Table 3. Irreducible Representations for Atomic Orbitals in the $D_{\infty h}$, D_{4h}, and D'_{4h} Double Group[a]

	s	p_x, p_y	p_z	d_{z^2}	d_{xz}, d_{yz}	d_{xy}	$d_{x^2-y^2}$	f_{z^3}	f_{xz^2}, f_{yz^2}	f_{xyz}	$f_{z(x^2-y^2)}$	$f_{x(x^2-3y^2)}$, $f_{y(3x^2-y^2)}$
$D_{\infty h}$	σ_g^+	π_u	σ_u^+	σ_g^+	π_g	δ_g		σ_u^+	π_u	δ_u		ϕ_u
D_{4h}	a_{1g}	e_u	a_{2u}	a_{1g}	e_g	b_{2g}	b_{1g}	a_{2u}	e_u	b_{1u}	b_{2u}	e_u
$D'_{4h}(SO)$	e'_g	e''_u, e'_u	e'_u	e'_g	e''_g, e'_g	e''_g	e''_g	e'_g	e''_u, e'_u	e''_u	e''_u	e''_u, e'_u

[a]NB the degeneracy of the δ symmetry orbitals is lifted shifting from linear to four-fold symmetry.

Table 4. Energies and Relative Intensities (F_D = dipole, F_Q = Quadrupole) of the Transitions to the Various Virtual Spinors[a]

spinor	$5f\delta_{3/2}$	$5f\phi_{5/2}$	$5f\delta_{5/2}$	$5f\phi_{7/2}$	$5f\pi_{1/2}$	$5f\pi_{3/2}$	$5f\sigma$	$6d_{xy}$	$6d_{x^2-y^2}$	$6d\pi_{1/2}$	$6d_{z^2}$	$6d\pi_{3/2}$
rel. energy/eV $(2p_{3/2})^{-1}(5f/6d)^1$	0	0.08	0.81	0.92	1.77	2.15	4.95	5.21	5.89	5.89	6.22	6.22
rel. energy/eV $(2p_{3/2})^{-1}$	0	0.22	0.84	0.99	1.97	2.31	4.98	4.98	7.03	7.45	7.64	7.74
rel. intensity	14.3	14.3	14.3	14.3	14.3	14.3	14.3	576	576	576	576	576
F_Q (perpendicular, 90°)	2.50	7.50	2.50	7.50	0.50	0.50	0.00					
F_Q (parallel, 0°)	5.00	0.00	5.00	0.00	4.00	4.00	3.00					
F_D (perpendicular, 90°)								3.00	3.00	1.50	1.00	1.50
F_D (parallel, 0°)								0.00	0.00	3.00	4.00	3.00

[a]"Perpendicular, 90°" and "parallel, 0°" refer to [...] orientation between uranyl cation and ε, respectively.

illustrate this effect most clearly, since the [splitting] is found to be largely independent of the presence or absence of a core hole. When the excited electron remains bound ($2p_{3/2}^{-1}5f_{xyz}^1$ and $2p_{3/2}^{-1}6d_{xy}^1$ in Figure 5), the relative energies of the various components within the 5f manifold and within the 6d manifold are essentially independent of the nature of the configuration. In contrast, in the fully ionized case (far right column) there is a striking increase of the tetragonal field splitting of the $6d_{xy}$ and $6d_{x^2-y^2}$. This presumably results from the $6d_{x^2-y^2}$ orbital becoming strongly σ-antibonding when its absolute energy (along with the other metal-based MOs) is lowered relative to that of the equatorial chloride ligands.

The total SCF energies of the $2p_{3/2}^{-1}5f_{xyz}^1$, and $2p_{3/2}^{-1}6d_{xy}^1$ configurations are found to differ by 4.844 eV, so the virtual energies of the latter configuration have been shifted upward to establish this difference, instead of being represented relative to the HOMO. The relative energies of various $2p_{3/2}^{-1}5f$ excited states are then taken relative to the energy of $2p_{3/2}^{-1}5f_{xyz}^1$, while those of the various $2p_{3/2}^{-1}6d$ excited states are taken relative to the energy of $2p_{3/2}^{-1}6d_{xy}^1$. Table 1 summarizes the energies and relative intensities of the transitions to the various virtual spinors using this $2p_{3/2}^{-1}(5f/6d)^1$ model and compares these to the equivalent relative energies for the fully ionized case $(2p_{3/2}^{-1})$. The symmetry labels used in Table 1 are not those of the D'_{4h} double group used in Figure 3, rather they are intended to indicate the principal orbital parentage, either in $D_{\infty h}$ or D_{4h} (Table 3).

3.3. Comparison between ADF and Experimental Results. The results of simulations using the data in Table 4 and a Lorentzian line width of 3.4 eV for 0° and 90° are shown in Figure 6. While the general shape of the L_3-edge spectra appears satisfactory, the dipolar intensity in the calculated parallel polarization is larger than for the calculated perpendicular polarization, which contrasts experimental observation (Figure 1). The dipolar intensity in the parallel polarization is dominated by transitions to 6dπ and 6dσ orbitals. Eigenvectors show that covalency is small except for 6dπ and 6dσ; the former interacts strongly with both oxygen and chlorine π-orbitals and the latter with oxygen orbitals. To mimic this, the intensity of transitions to these orbitals was reduced by a factor of 0.7 to account qualitatively for the attenuation of their metal character introduced by covalency.

The main features of these simulations agree satisfactorily with the experimental spectra (see Figure 6b and c): higher intensity and lower relative energy position of the spectrum in the 90° versus the 0° geometry. In particular, the relative intensity of the quadrupole allowed transitions to the 5f shell compared to the dipole allowed transitions to the 6d shell is well-reproduced.

The 0.5 eV difference between the absorption maxima in the parallel and perpendicular polarizations using the $(2p_{3/2})^{-1}(5f/6d)^1$ model and including covalence in Figure 6 can be compared to the experimental difference of 0.9 ± 0.1 eV. This difference reflects the fact that the barycenter of the $6d_{xy}$ and $6d_{x^2-y^2}$ orbitals, to which transitions are forbidden in the parallel polarization, lies ~0.6 eV below that of the 6dπ and 6dσ components. The substantially larger width of the 90° spectrum is primarily due to the tetragonal field splitting of the $6d_{xy}$ and $6d_{x^2-y^2}$ orbitals. Indeed, a shoulder can be discerned on the rising edge of the experimental spectrum at about 17172 eV (feature B′), consistent with this description. The simulation does not reproduce well the separation between the barycenters of the 5f and 6d absorption regions: ~5.2 eV compared to the experimental separation of 7.0 eV (25°)/7.7 eV (90°) (see Table 1). In the perpendicular case, the dominant intensity occurs from transitions to 5fδ and 5fφ, which are nearly degenerate and ~2.5 eV lower in energy than 5fπ. These transitions are most likely to be detectable on the low energy side of the intense dipole-allowed transitions to the 6d shell. Indeed, the pre-edge feature of the 90° spectrum is found at −1.5 eV ± 0.1 eV lower energy position compared to the 25° spectrum, whereas the peak area remains similar (Figure 2, Table 1). The limitations of the DFT method are revealed by the calculated value for the excitation energy, 17 623 eV, compared to the experimental value, 17 169 eV, a difference of 2.6%.

Calculations with a hole in the 3d shell give a very similar pattern of energy levels for excitation to 5f, 6d, and ionization (see Supporting Information Table S1). The assignments of the U M_4-edge PD-HR-XANES absorption resonances in section 3.1 are confirmed by ADF (see Table 4 and Supporting Information Table S1). Peak D in the U M_4-edge PD-HR-XANES spectrum for the $\alpha = \alpha_1 + 5°$ ($0 \leq \alpha_1 \leq 45°$) geometry (see Supporting Information Figure S5) exhibits asymmetric shape, evidence for transitions to 5fδ and 5fφ orbitals with
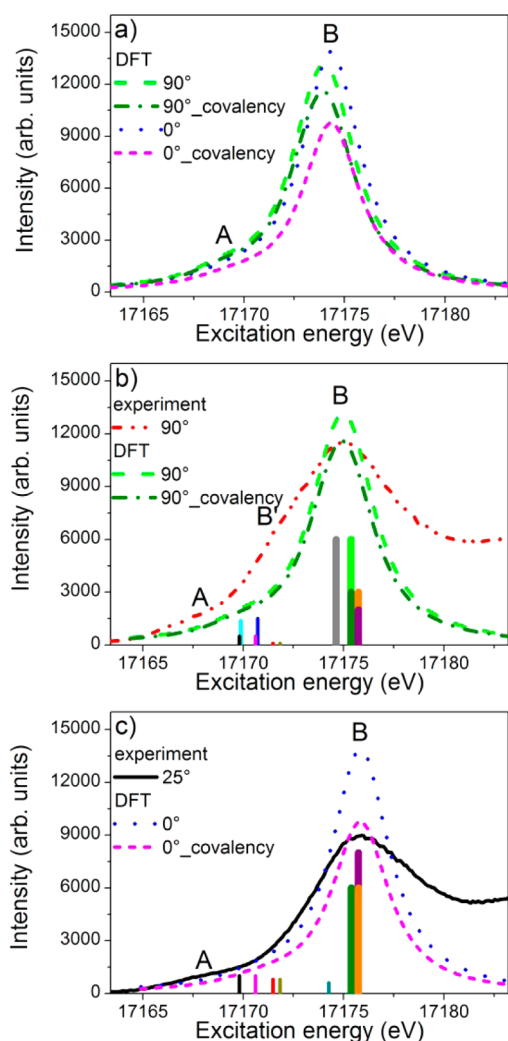
Figure 6. DFT calculated U L_3-edge PD-HR-XANES spectra for the 90° and 0° geometry (a). DFT calculated and experimental U L_3-edge PD-HR-XANES spectra and relative oscillatory strengths for $2p_{3/2} \rightarrow 5f$ (thin bars) and $2p_{3/2} \rightarrow 6d$ transitions (thick bars) for the 90° (b) and 0° geometry (c). The unoccupied orbitals are marked with different colors: $5f\delta_{3/2}$ (black), $5f\phi_{5/2}$ (cyan), $5f\delta_{5/2}$ (magenta), $5f\phi_{7/2}$ (blue), $5f\pi_{1/2}$ (red), $5f\pi_{3/2}$ (dark yellow), $5f\sigma$ (dark cyan), $6d_{xy}$ (gray), $6d_{x^2-y^2}$ (green), $6d\pi_{1/2}$ (olive), $6d_{z^2}$ (purple), $6d\pi_{3/2}$ (orange). For clarity the $2p_{3/2} \rightarrow 5f$ intensities are multiplied by 4 therefore they deviate from the 2.48% $2p_{3/2} \rightarrow 6d$ relative intensity reported in Table 4.

about 0.6 eV energy separation. The ground state calculation with and without spin−orbit interaction yields about 0.1 and 0.8 eV energy separation between $5f\delta$ and $5f\phi$ orbitals, respectively, essentially unaffected by the presence of $3d_{3/2}$ core-hole (see Table 4 and Supporting Information Table S1). $5f\delta_{3/2}$ and $5f\phi_{5/2}$ are nearly degenerate, as well as $5f\delta_{5/2}$ and $5f\phi_{7/2}$. The experimental and theoretical results suggest that spin−orbit interaction is required to reproduce the experimentally observed energy difference.

The integral intensities of the D, E, and F absorption resonances averaged over the U M_4-edge PD-HR-XANES spectra have ratio 5:3.5:1, which deviates from the theoretically predicted 4:2:1. This difference needs to be addressed in future systematic U M_4-edge studies of model powder compounds. Self-absorption effects might also have an influence on peak intensities; therefore, for quantitative analyses, their careful

assessment is required. However, in our case at hand such effects do not significantly contribute to our spectra, as comparison to spectra of diluted materials with low U concentration has shown.

In the M_4-edge spectra the oscillatory strength of transitions to δ and ϕ orbitals change significantly (D), whereas the transitions to π (E) and σ (F) orbitals remain very similar within the probed 40° angular range. As reported in Table 4 the relative quadrupole intensities (see Figure 6 b and c) of transitions to π and σ orbitals should increase. This is not observed in the M_4-edge experimental spectra and might be attributed to too small relative intensity changes for 40° change. The contribution of transitions to π and σ orbitals is clearly visible in the L_3-edge spectra as the barycenter of the pre-edge peak shifts to higher energies going from the 90° to the 0° geometry, which confirms that the L_3 and M_4-edge results are consistent.

3.4. FEFF9.6 Calculations. The U L_3-edge PD-HR-XANES spectra calculated with the FEFF9.6 code are shown in Figure 7. The spectra calculated for the 90° or 0° geometry including
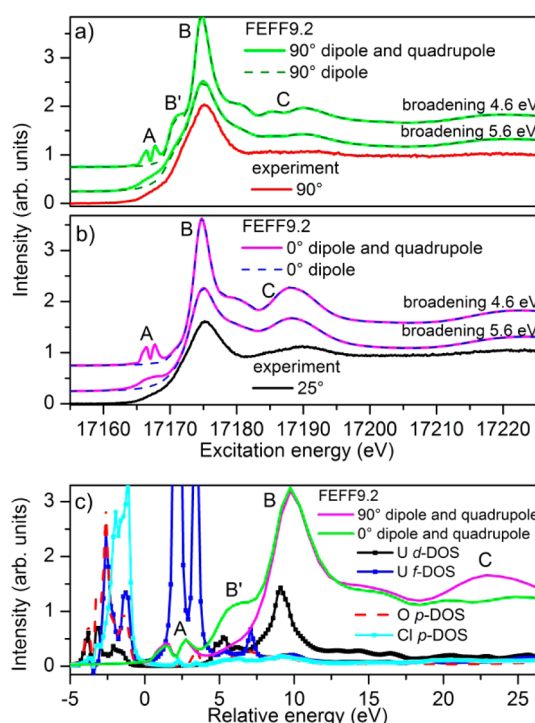

Figure 7. FEFF9.6 calculated with 4.6 and 5.6 eV broadening and experimental U L_3-edge PD-HR-XANES for the 90° (a) and 0° geometry (b); FEFF9.6 calculated U L_3-edge PD-HR-XANES for the 90° and 0° geometry (broadening 4.6 eV) and U, O, Cl DOS (c).

only dipole allowed $(2p_{3/2} \rightarrow 6d)$ electronic transitions reproduce the overall shape of the experimental spectra well, with exception of absorption resonance A (Figure 7a, b). Feature A gains significant intensity by considering quadrupole transitions $(2p_{3/2} \rightarrow 5f)$ in the calculations. By comparing spectra with the U f- and d-density of states (DOS) in Figure 7 c, it is apparent that f-DOS has strong intensity in this pre-edge region, whereas there is no significant d-DOS contribution. This observation agrees with ADF results and previous studies.[22,25] The d-DOS describes the remaining part of the spectrum well, as expected from dipole selection rules. Note that no polarization dependency is included in the DOS

calculations. Comparison to the ADF calculation results allow us to assign feature B′ to electronic $2p_{3/2} \rightarrow 6d_{xy}$ transitions with significant oscillatory strength in the perpendicular geometry, manifested by an asymmetric shape of the experimental 90° WL. These transitions are not observed in the parallel geometry spectrum shown in Figure 5b, as also found by ADF (Table 1). Feature C gains intensity in the parallel case, which implies ε was directed along the UO_2^{2+} molecule axis. The FEFF9.6 calculations reproduce well the energy positions of all spectral features and their relative intensities by adding 5.6 eV broadening into the simulations to account for both experimental and core−hole lifetime broadening.

4. CONCLUSIONS

Our ADF and FEFF9.6 calculations demonstrate that the pre-edge observed in the experimental U L_3-edge PD-HR-XANES spectra originates mainly from weak $2p_{3/2} \rightarrow 5f$ transitions. Additionally, no electronic transitions to the $6d_{xy}$ orbital are present when ε is aligned with the uranyl moiety. This theoretical result was experimentally confirmed for the first time and is manifested in the experimental U L_3-edge PD-HR-XANES recorded at a 90° geometry (perpendicular relation between uranyl cation and ε) by an asymmetry (feature B′ in Figures 6 and 7), larger area and energy shift to lower energies of the WL; B′ is absent in the 0° PD-HR-XANES.

The low intensity of the broad pre-edge and its overlap with the intense main $2p_{3/2} \rightarrow 6d$ dipole transitions prevent accurate estimation of mixing of ligand with metal f orbitals from conventional spectra. The increased energy resolution of HR-XANES allows a pre-edge from the main absorption transitions to be distinguished. Comparison of experimental results with spectra simulated using our ADF calculations with and without the inclusion of covalence, strongly suggests the existence of covalent bonding between the U and the ligands with about 30% mixing of $6d\pi$ and $6d\sigma$ with O and Cl valence orbitals. The spin−orbit interaction, taken into account in both ADF and FEFF9.6 codes, mainly introduces splitting of $5f\delta$, $5f\phi$, and $5f\pi$ states and its inclusion is prerequisite to accurate interpretation of U M_4-edge HR-XANES spectra. The comparatively large broadening in U L_3 edge HR-XANES prevents detection of these split f states in the pre-edge region. The FEFF9.6 code is accurate in performing U L_3-edge HR-XANES calculations and reliably reproduces the edge and the post edge regions. Our results should encourage its application in future electronic and geometric structural investigations of actinide materials. On the basis of the example we have provided here, the combination of this as a tool and the HR-XANES technique will increase the degree of accuracy in probing actinide electronic structure in future studies and thereby stimulate development of theoretical codes.

■ ASSOCIATED CONTENT

S **Supporting Information**

Computational details, experimental details, and analyses of U L_3-edge extended X-ray absorption fine structure (EXAFS) spectra. This material is available free of charge via the Internet at http://pubs.acs.org.

■ AUTHOR INFORMATION

Corresponding Author

*E-mail: Tonya.Vitova@kit.edu.

Present Address

△M.A.D.: Dalton Nuclear Institute, The University of Manchester, Manchester, M13 9PL, United Kingdom.

Notes

The authors declare no competing financial interest.

■ ACKNOWLEDGMENTS

■ REFERENCES

(1) Grenthe, I.; Drożdżynński, J.; Fujino, T.; Buck, E.; Albrecht-Schmitt, T.; Wolf, S. Uranium. In *The Chemistry of the Actinide and Transactinide Elements*; Morss, L., Edelstein, N., Fuger, J., Eds.; Springer: Netherlands, 2006; pp 253−698. Denecke, M.; Nolf, W.; Rack, A.; Tucoulou, R.; Vitova, T.; Falkenberg, G.; Abolhassani, S.; Cloetens, P.; Kienzler, B. Speciation of Actinides in Granite Subjected to Tracer Studies. In *Actinide Nanoparticle Research*; Kalmykov, S. N., Denecke, M. A., Eds.; Springer: Berlin, 2011; pp 413−435. Geckeis, H.; Lützenkirchen, J.; Polly, R.; Rabung, T.; Schmidt, M. *Chem. Rev.* **2013**, *113* (2), 1016−1062. Altmaier, M.; Gaona, X.; Fanghänel, T. *Chem. Rev.* **2013**, *113* (2), 901−943. Walther, C.; Denecke, M. A. *Chem. Rev.* **2013**, *113* (2), 995−1015.

(2) Panak, P. J.; Geist, A. *Chem. Rev.* **2013**, *113* (2), 1199−1236.

(3) Barker, T. J.; Denning, R. G.; Thorne, J. R. G. *Inorg. Chem.* **1987**, *26* (11), 1721−1732. Pepper, M.; Bursten, B. E. *Chem. Rev.* **1991**, *91* (5), 719−741. Schreckenbach, G.; Hay, P. J.; Martin, R. L. *J. Comput. Chem.* **1999**, *20* (1), 70−90. Matsika, S.; Pitzer, R. M. *J. Phys. Chem. A* **2000**, *105* (3), 637−645. Kaltsoyannis, N. *Chem. Soc. Rev.* **2003**, *32* (1), 9−16. Clark, A. E.; Sonnenberg, J. L.; Hay, P. J.; Martin, R. L. *J. Chem. Phys.* **2004**, *121* (6), 2563−2570. Pierloot, K.; van Besien, E. *J. Chem. Phys.* **2005**, *123* (20), -. Réal, F.; Vallet, V.; Marian, C.; Wahlgren, U. *J. Chem. Phys.* **2007**, *127* (21), -. Liu, G.; Deifel, N. P.; Cahill, C. L.; Zhurov, V. V.; Pinkerton, A. A. *J. Phys. Chem. A* **2011**, *116* (2), 855−864. Zhurov, V. V.; Zhurova, E. A.; Stash, A. I.; Pinkerton, A. A. *J. Phys. Chem. A* **2011**, *115* (45), 13016−13023. Tecmer, P.; Bast, R.; Ruud, K.; Visscher, L. *J. Phys. Chem. A* **2012**, *116* (27), 7397−7404. Dau, P. D.; Su, J.; Liu, H.-T.; Huang, D.-L.; Li, J.; Wang, L.-S. *J. Chem. Phys.* **2012**, *137* (6), -. Gomes, A. S. P.; Jacob, C. R.; Real, F.; Visscher, L.; Vallet, V. *Phys. Chem. Chem. Phys.* **2013**, *15* (36), 15153−15162. Schnaars, D. D.; Wilson, R. E. *Inorg. Chem.* **2013**, *52* (24), 14138−14147.

(4) Denning, R. G. *Struct. Bonding (Berlin)* **1992**, *79*, 215−276.

(5) Denning, R. G. *J. Phys. Chem. A* **2007**, *111* (20), 4125−4143.

(6) Spencer, L. P.; Yang, P.; Minasian, S. G.; Jilek, R. E.; Batista, E. R.; Boland, K. S.; Boncella, J. M.; Conradson, S. D.; Clark, D. L.; Hayton, T. W.; Kozimor, S. A.; Martin, R. L.; MacInnes, M. M.; Olson, A. C.; Scott, B. L.; Shuh, D. K.; Wilkerson, M. P. *J. Am. Chem. Soc.* **2013**, *135* (6), 2279−2290.

(7) Templeton, D. H.; Templeton, L. K. *Acta Crystallogr. A* **1982**, *38* (Jan), 62−67.

(8) Hudson, E. A.; Allen, P. G.; Terminello, L. J.; Denecke, M. A.; Reich, T. *Phys. Rev. B* **1996**, *54* (1), 156−165.

(9) Denning, R. G.; Green, J. C.; Hutchings, T. E.; Dallera, C.; Tagliaferri, A.; Giarda, K.; Brookes, N. B.; Braicovich, L. *J. Chem. Phys.* **2002**, *117* (17), 8008−8020.

(10) Fonseca Guerra, C.; Snijders, J. G.; te Velde, G.; Baerends, E. J. *Theor. Chem. Acc.* **1998**, *99* (6), 391−403. te Velde, G.; Bickelhaupt, F.

M.; Baerends, E. J.; Fonseca Guerra, C.; van Gisbergen, S. J. A.; Snijders, J. G.; Ziegler, T. *J. Comput. Chem.* **2001**, *22* (9), 931−967.

(11) Rehr, J. J.; Kas, J. J.; Vila, F. D.; Prange, M. P.; Jorissen, K. *Phys. Chem. Chem. Phys.* **2010**, *12* (21), 5503−5513.

(12) Ohwada, K. *Spectrochim Acta A* **1975**, *31* (7), 973−977. Hall, D.; Rae, A. D.; Waters, T. N. *Acta Crystallogr.* **1966**, *20*, 160−&.

(13) Glatzel, P.; Bergmann, U. *Coord. Chem. Rev.* **2005**, *249* (1−2), 65−95.

(14) Baerends, E. J. *ADF Program System*, version 2000.02; Vrije Universiteit: Amsterdam, 2000.

(15) Baerends, E. J.; Ellis, E. G.; Ros, P. *Chem. Phys.* **1973**, *2*, 41. te Velde, B.; Baerends, E. J. *J. Comput. Phys.* **1992**, *99*, 84.

(16) van Lenthe, E.; van Leeuwen, R.; Baerends, E. J.; Snidgers, J. G. *Int. J. Quantum Chem.* **1996**, *57*, 281. van Lenthe, E.; Snidgers, J. G.; Baerends, E. J. *J. Chem. Phys.* **1996**, *105*, 6505.

(17) Vosko, S. H.; Wilk, L.; Nusair, M. *Can. J. Phys.* **1980**, *58*, 1200.

(18) Becke, A. D. *Phys. Rev. A* **1988**, *38*, 3098.

(19) Perdew, J. P. *Phys. Rev. B* **1986**, *33*, 8822.

(20) Vitova, T.; Denecke, M. A.; Göttlicher, J.; Jorissen, K.; Kas, J. J.; Kvashnina, K.; Prüßmann, T.; Rehr, J. J.; Rothe, J. *J. Phys.: Conf. Ser.* **2013**, *430* (1), No. 012117.

(21) de Groot, F. M. F.; Krisch, M. H.; Vogel, J. *Phys. Rev. B* **2002**, *66* (19), No. 195112.

(22) Vitova, T.; Kvashnina, K. O.; Nocton, G.; Sukharina, G.; Denecke, M. A.; Butorin, S. M.; Mazzanti, M.; Caciuffo, R.; Soldatov, A.; Behrends, T.; Geckeis, H. *Phys. Rev. B* **2010**, *82* (23), No. 235118.

(23) Petiau, J.; Calas, G.; Petitmaire, D.; Bianconi, A.; Benfatto, M.; Marcelli, A. *Phys. Rev. B* **1986**, *34* (10), 7350−7361.

(24) Fillaux, C.; Berthet, J. C.; Conradson, S. D.; Guilbaud, P.; Guillaumont, D.; Hennig, C.; Moisy, P.; Roques, J.; Simoni, E.; Shuh, D. K.; Tyliszczak, T.; Castro-Rodriguez, I.; Den Auwer, C. *C. R. Chim.* **2007**, *10* (10−11), 859−871.

(25) Walshe, A.; Prussmann, T.; Vitova, T.; Baker, R. J. *Dalton Trans.* **2014**, *43* (11), 4400−4407.